

## Modelling of an inductive sensor of the Foucault cardiogram

Jüri Vedru<sup>a</sup>, Rauno Gordon<sup>b</sup>, Leo Henn Humal<sup>c</sup> and Jaanus Trola<sup>d</sup>

<sup>a</sup> Institute of Physics, University of Tartu, Tähe 4, 51010 Tartu, Estonia; juri.vedru@ut.ee

<sup>b</sup> Thomas Johann Seebeck Department of Electronics, Tallinn University of Technology, Ehitajate tee 5, 19086 Tallinn, Estonia

<sup>c</sup> Humal Elektroonika OÜ, Riia 24, 51010 Tartu, Estonia

<sup>d</sup> University of Tartu, Ülikooli 18, 50090 Tartu, Estonia

Received 5 April 2011

**Abstract.** An electric circuit model, describing the inductive sensor of cardiac mechanical activity in its working condition, has been developed. The sensor includes a single-turn inductor coil, which is considered to be attached to the thoracic surface of a man, in front of the heart. The coil is fed by 7.7 MHz constant current and induces probing eddy currents in the body. A simple axisymmetric computer model of the thorax, formed of tightly packed circular current tubes, was created to represent the coil–patient system. With complex-valued impedivities for the body tissues, the model has been used to calculate the impedances and inductances within the system. For comparison, a fine FEM model of the same system was created and tested. Comparable results of the two different calculation methods exhibited sufficient consistence. The estimates of the parameters of the system were found and the signal production was analysed.

**Key words:** Foucault cardiography, induction cardiography, model of thorax, heart, electrical bioimpedance, eddy currents.

### 1. INTRODUCTION

In induction methods for electrical impedance measurement and tracking [<sup>1,2</sup>], the probing currents are applied in the form of Foucault or eddy currents, using inductors. The same inductors can be used as signal receivers, thus forming sensors for inductive measurement. To improve the induction methods, identified models of such sensors are necessary. The present study is based on a concrete example of the Foucault cardiographic sensor, which is applied to track heart mechanical activity [<sup>2,3</sup>]. The objective of the present work was to develop a realistic but simple computer model of the sensor loaded with a patient and, using

the model, to study the factors, which determine the origination of the signal in the induction method for tracking the heart.

## 2. THE INDUCTIVE SENSOR

The example sensor includes a shielded single-turn inductor coil (Fig. 1). The coil is 13.4 cm in diameter and made of copper wire with a rectangular  $10 \times 2$  mm cross-section. Together with a capacitor it forms an LCR oscillatory circuit (Fig. 2) with a resonance frequency of 7.7 MHz. The inductor is electrically shielded by a grounded box-like surrounding. The shielding box is made of 1 mm thick foil-clad laminate that has been extra engraved to disable eddy currents in it. The sensor is assumed to be attached to the thoracic surface of a normal human male just in front of the heart.

A single-frequency example Foucault cardiograph, incorporating the sensor, operates at the resonance frequency of this oscillatory circuit. It consists of a sensor-based soft-regime LC-oscillator, which oscillates at the resonance frequency of the sensor, an amplitude detector and a low-frequency signal amplifier. The high-frequency voltage on the sensor and thus the low-frequency output of the detector are modulated by the impedance and reflected from the inductively coupled attached burden. Since the latter varies with cardiac contractions, cardiac-related modulation of the reflected impedance results. Thus the sensor is applied in the cardiograph to convert variations of the burden impedance into variations of the reflected impedance.

Further in this paper, we will consider the variation of the reflected impedance as the output of the present sensor.

An excerpt from a Foucault cardiogram, recorded with the example Foucault cardiograph, is presented in Fig. 3.

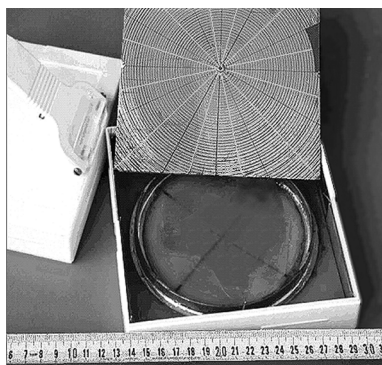


**Fig. 1.** The example sensor: inductor coil with the uncovered shielding in enclosure.

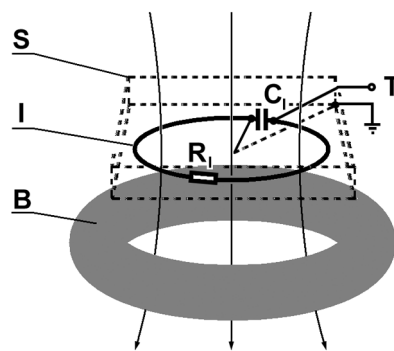


**Fig. 2.** The scheme of the situation studied: B – the eddy currents region (symbolic); I – the inductor coil; S – electrical shielding;  $R_1$  – the coil resistance (symbolic);  $C_1$  – primary circuit capacitance; T – outlet terminal of the sensor.

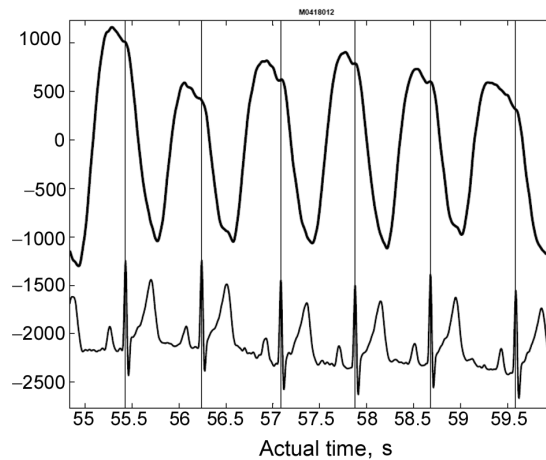


**Fig. 3.** Excerpt from a Foucault cardiogram, recorded with the example Foucault cardiograph. The curve above – Foucault cardiogram, the curve below – simultaneous electrocardiogram. Units on the vertical axis are arbitrary.

### 3. MODEL OF THE SENSOR

#### 3.1. Theoretical considerations

A static model with axisymmetric geometry (similar to the disk model used in [2,3]; Fig. 4) is applied to calculate the interaction between the inductor and the eddy currents. The eddy currents region of the body is modelled by a cylinder consisting of three parts filled with different homogeneous isotropic “tissues” – pulmonary, from the heart and from the thoracic wall. The material in the parts is considered to have tissue-specific complex-valued impedivity as is inherent to the biotissue. The situation is studied for eddy currents, induced by the inductor, which is fed from a constant sinusoidal current source at a fixed frequency.

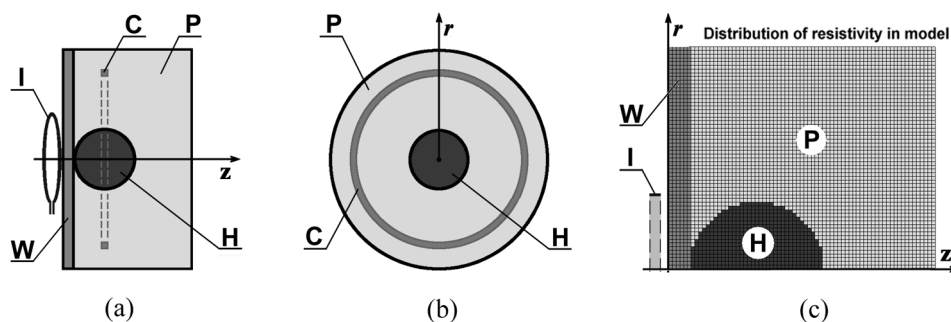


**Fig. 4.** The model of the eddy currents region of the body: (a) and (b) – lateral and frontal cross-sections of the model; (c) – the region of calculation: a half of the section of the model (case of  $n_z \times n_r = 72 \times 60$  secondary coils). I – inductor, W – thoracic wall, C – secondary coil, P – pulmonary tissue, H – heart.

First, to calculate the interaction, the cylinder, representing the region of eddy currents, is approximated by a dense-packed array of  $n = n_z \times n_r$  co-axial current tubes or elementary coils having equal small square cross-sections. The impedance of each elementary coil consists of its pure self-inductive component and a burden component due to the material of the coil.

Then the situation is changed, enabling interpretation in terms of two inductive-coupled coils or circuits (Fig. 2), consisting of a single-turn primary coil (the inductor) and a secondary one, the latter being the equivalent of the whole cylinder with eddy currents. Due to the peculiar properties of the material, some deviations from ordinary technical inductively coupled coils result.

At fixed topography, the distribution of currents is established in the eddy currents region. It has an influence on the equivalent characteristics of the array of secondary coils. Although the electromotive forces in all the elementary coils have the same phase, the currents there have different phase shifts determined by particular tissues involved. This feature causes differences between the present model with its complex impedivities and the model [4] with tissues having purely active resistivities. Starting now from the equal complex power  $\tilde{S}$  requirement

$$\tilde{S} = \mathbf{R}_{\text{II}} |\mathbf{I}_{\text{II}}|^2 = \sum_i \mathbf{R}_i |\mathbf{I}_i|^2, \quad (1)$$

where  $\mathbf{R}_{\text{II}}$  is the total burden impedance of the secondary circuit,  $\mathbf{R}_i$  and  $\mathbf{I}_i$  are the individual impedances of elementary coils (as conducting channels made of materials with complex-valued impedivity) and the currents in them, respectively,  $\mathbf{I}_{\text{II}} = \sum_{k=1}^n \mathbf{I}_k$  being the total current in the secondary circuit. Then the total burden impedance of the secondary circuit  $\mathbf{R}_{\text{II}}$  is calculated as

$$\mathbf{R}_{\text{II}} = \sum_{i=1}^n |\mathbf{K}_i|^2 \cdot \mathbf{R}_i, \quad (2)$$

where

$$\mathbf{K}_i = \mathbf{I}_i \left( \sum_{k=1}^n \mathbf{I}_k \right)^{-1}. \quad (3)$$

Here and below the bold characters stand for phasors. To enable compatibility with the formulae used in electric circuit theory for the description of inductively coupled coils, the notations have been kept the same as the conventional ones despite becoming complex-valued; e.g.,  $\mathbf{R}_i$  instead of  $\mathbf{Z}_i$  stands for a complex-valued burden impedance.

Similarly, the equivalent self-inductance of the secondary circuit and the equivalent mutual inductances between the inductor and the secondary circuit were calculated. Before establishing a single equivalent for the array of secondary coils, the values of self-inductances of the elementary coils and the mutual inductances between them had to be calculated.

To use the conventional formulae of inductances [5], intended for the calculation of inductive windings where the current has the same value in each of the turns, the diversity of the secondary (eddy) currents had to be substituted by an equivalent uniform current.

The equivalence means keeping the magnetic flux  $\Phi_i$  for each of the elementary coils. The flux of an elementary coil can be presented as

$$\Phi_i = \tilde{L}_i I_i = \tilde{L}_i \frac{I_i}{\frac{1}{n} \sum_{j=1}^n I_j} = n K_i \tilde{L}_i \frac{I_{\parallel}}{n}, \quad (4)$$

where  $\tilde{L}_i$  marks the self-inductance of the coil standing alone and  $n$  is the total number of elementary coils in the object.  $I_{\parallel}/n$  comprises the uniform value substituted for the current in the secondary elementary coils while the total secondary circuit current  $I_{\parallel} = \sum_{j=1}^n I_j$  remains unchanged after its uniforming. It can be concluded from Eq. (4) that the weighted inductances should be calculated by the formula  $L_i = n K_i \tilde{L}_i$ . Further, to transfer inductances, calculated for a multiple-turn coil, into inductances for a massive conductor with the same geometry and current distribution, the results should be divided by  $n^2$  [5]. Therefore, the self-inductances of the elementary coils in the secondary coil array is calculated as follows:

$$L_i = \frac{K_i}{n} \tilde{L}_i. \quad (5)$$

Similar weighting occurs with coils when multiple turns of the current are placed into the same geometric region. Therefore the multiplier  $K_i/n$ , which conforms with the number of coil turns squared at mutual inductance calculation, leads to the following weighting:

$$M_{ij} = \frac{1}{n} \sqrt{K_i K_j} \tilde{M}_{ij}. \quad (6)$$

Here  $M_{ij}$  is the equivalent mutual inductance of a couple of elementary coils, isolated from the secondary coil array after the current distribution is changed to uniform and  $\tilde{M}_{ij}$  is the mutual inductance of the same couple without weighting. The stand-alone values  $\tilde{L}_i$  and  $\tilde{M}_{ij}$  are calculated using available formulae, for instance, in [5]. The same approach is used to calculate the mutual inductances between the secondary coils and the inductor coil.

Due to the complex values of  $K_i$ , complex values obtain also  $R_i$ ,  $L_i$  and  $M_{ij}$ . This is a remarkable uncommon phenomenon.

The equivalent total self-inductance of the secondary circuit  $L_{\parallel}$  is expressed as [5]

$$L_{\parallel} = \frac{1}{n^2} \left( \sum_{i=1}^n L_k + \sum_{i=1}^n \sum_{j=1}^n M_{ij} \right), \quad i \neq j. \quad (7)$$

Skin effect was supposed to cause concentration of the inductor currents into the opposite narrow sides of the inductor coil's surface. Therefore, the inductor is modelled as two equal threads of the current. The equivalent mutual inductance between the primary and the secondary circuit  $M_{I,II}$  is expressed as

$$M_{I,II} = \frac{1}{n \cdot 2} \sum_{i=1}^n (M_{i,prox} + M_{i,dist}), \quad (8)$$

where  $M_{i,prox}$  and  $M_{i,dist}$  are the mutual inductances between the secondary coils and either proximal or distal current threads in the inductor coil, calculated according to Eq. (6).

Distribution of the currents in secondary coils, which is necessary in Eq. (3) to find the factors  $K_i$ , is estimated ignoring the backward influence of the magnetic field of the induced currents (i.e., the inductive reactances of the elementary coils). Calculation of the corresponding electromotive forces has been presented in [6]. The currents are obtained using the Ohm's Law.

The inductive sensor transforms the secondary circuit impedance into the reflected impedance  $\Delta Z_1$  in the primary circuit, in series with the self-impedance  $Z_{1,0}$  of the unloaded coil:

$$Z_1 = Z_{1,0} + \Delta Z_1, \quad (9)$$

where  $Z_1$  means the impedance of the inductor coil when attached to the patient.

The reflected impedance can be found using the mutual inductance model of the coreless transformer, which leads to the following well-known [7] formula, but where the parameters now are complex-valued (phasors):

$$\Delta Z_1 = \frac{4\pi^2 f_w^2 M_{I,II}^2}{R_{II} + i2\pi f_w L_{II}}, \quad (10)$$

where  $f_w$  is the working frequency of the sensor.

Notice that in the present case, due to complex values of  $R_{II}$  and  $L_{II}$ , the addenda in the right-side denominator of Eq. (10) are not the denominator's real and imaginary parts.

### 3.2. Determination of the model parameters

For the actualization of the model, the dimensions of the inductor, as well as its electric properties while having no load were either measured on the example sensor or calculated for it (Table 1). The active resistance  $R_{1,0}$  of the unloaded inductor coil was found in the process of FEM calculations, which are described below. The procedure accounts for the skin effect in the coil wire.

The capacitances from the shielding to the inductor and to the body,  $C_S \cong 40$  pF and  $C_B \cong 140$  pF, were measured on the example sensor. Due to its relatively small value,  $C_S$  in the present sensor only weakly influences the

**Table 1.** Electric properties of the example sensor

Properties	Notations	Values
Active self-resistance of the unloaded inductor coil (calculated using FEM)	$R_{L0}$	17.84 m $\Omega$
Self-inductance of the unloaded inductor coil (calculated)	$L_{L0}$	238.2 nH
Capacitance of the capacitor in the primary circuit (measured)	$C_1$	1800 $\pm$ 20 pF
Capacitance between the shielding and the inductor (measured)	$C_S$	~40 pF
Capacitance between the shielding and the patient's body (measured)	$C_B$	~140 pF

primary circuit's parallel capacitance. The other one,  $C_B$ , in a geometrically symmetric model should not act at all. Though in real asymmetric cases it would cause a certain amount of noise if changed, in the present model this is not the case.

The dimensions of the body disk and its contents (Table 2) were roughly derived from a normal adult person. Determination of the impedivities for the regions of the body disk was an intricate task. Combining the available values for tissues at the working frequency of the sensor [8], estimates of these impedivities have been derived (Table 2 and Fig. 5).

The set of non-alternative values of the parameters in Tables 1 and 2 comprises the basic case of the model set-up.

**Table 2.** Geometrical and impedivity specifications of the model

Parameters	Values		
Diameter of the	body disk 40.0 cm	inductor coil* <i>basic set-up:</i> 13.4 cm <i>alternatives:</i> 6.7 cm 20.1 cm	heart 12.0 cm
Thickness of the	whole body disk 24.0 cm	thoracic wall 2.0 cm	
Other characteristics of the inductor	the gap between the inductor's rim and thoracic surface 0.7 cm	coil wire width 1.0 cm	coil wire thickness 0.2 cm
Impedivity of the	heart 1.35 $\Omega\cdot\text{m}$ $\angle -12.9^\circ$	thoracic wall** <i>basic set-up:</i> 3.23 $\Omega\cdot\text{m}$ $\angle -13.8^\circ$ <i>alternatives:</i> 2.43 $\Omega\cdot\text{m}$ $\angle -11.1^\circ$ 1.63 $\Omega\cdot\text{m}$ $\angle -8.4^\circ$	pulmonary region 3.19 $\Omega\cdot\text{m}$ $\angle -14.8^\circ$

\* The 13.4 cm coil diameter (the case of the example sensor coil, marked by D in Figs. 9 and 10) is the basic case, the alternatives were used for comparative study.

\*\* The basic value of the thoracic wall impedivity was used in the basic set-up of the model, the alternatives served for comparative study.

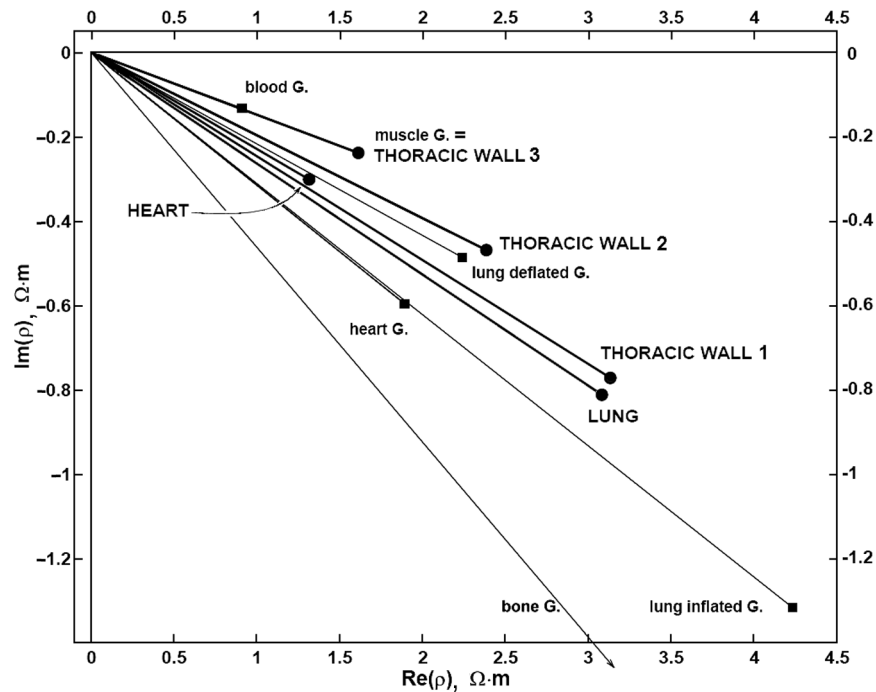


**Fig. 5.** Diagram of the tissue impedivities used in the model. The literature data from [8] are represented by squares and thin vector lines; corresponding labels end with “G.”. The derived impedivities are represented by circles and bold vector lines; corresponding labels are printed with capital letters.

The proper value for the effective impedivity of the thoracic wall remained questionable; therefore two additional runs of the model calculations with alternative values of impedivity were performed. One of the alternative values, the value with the least modulus, equals to the impedivity of pure skeletal muscle; the other alternative is a value chosen between the basic and the pure muscular ones.

Though the diameter of the inductor coil in the example sensor was well known, to study the influence of its size on the properties of the sensor, further two additional runs of the model calculations with two alternative values for the inductor diameter were pursued.

## 4. CALCULATIONS OF THE MODEL

### 4.1. Studies of the model using MATLAB

The majority of the model calculations have been performed using special software, which was composed in MATLAB.



The sensor is expected to be a part of a self-oscillating device, which works in resonance with the sensor oscillatory circuit. Therefore it was natural to calculate the properties of the sensor just at its resonance frequency  $f_w = 7.686$  MHz at working conditions when it is loaded with a patient. The frequency was known from the measurement on the example sensor. The body disk was taken as an array, consisting of  $n_z \times n_r = 72 \times 60$  elementary secondary coils ( $\Delta z = \Delta r = 1/3$  cm).

The values for the electric properties have been obtained for the unloaded sensor as well as for the circuitry, loaded by the static body disk. In Table 3, one can see some features of the electric properties of the inductor, loaded by an object, composed of biological tissues.

**Table 3.** Values of the properties of the sensor obtained in the static model for the basic set-up\*

Property	Notation	Value
Resistance of the <i>unloaded</i> inductor coil (from Table 1)	$R_{I,0}$	17.84 m $\Omega$
Inductance of the <i>unloaded</i> inductor coil (from Table 1)	$L_{I,0}$	238.2 nH
Reactance of the <i>unloaded</i> inductor coil at the working frequency of the loaded sensor	$\rho_0 = 2\pi f_w L_{I,0}$	11.504 m $\Omega$
Impedance of the <i>unloaded</i> inductor coil at the working frequency of the loaded sensor	$Z_{I,0}$	11.504 m $\Omega$ $\angle 89.92^\circ$
Capacitance in the primary circuit (from Table 1)	$C_1$	1.80 nF
Estimate for the quality factor of the unloaded sensor	$Q_0$	644
Working frequency (i.e. resonance frequency) of the loaded sensor (measured)	$f_w$	7.686 MHz
“Complex burden resistance” of the secondary circuit	$R_{II}$	67 020 m $\Omega$ $\angle -14.23^\circ$
“Complex inductance” of the secondary circuit	$L_{II}$	51.27 nH $\angle 0.41^\circ$
corresponding impedance	$i2\pi f_w L_{II}$	2.476 m $\Omega$ $\angle (90 + 0.41)^\circ$
“Complex mutual inductance” between the primary and secondary circuits	$M_{I,II}$	38.11 nH $\angle 0.10^\circ$
corresponding impedance	$i2\pi f_w M_{I,II}$	1841 m $\Omega$ $\angle (90 + 0.10)^\circ$
Impedance of the secondary circuit	$Z_{II}$	66 440 m $\Omega$ $\angle -12.17^\circ$
Impedance reflected into the inductor	$\Delta Z_I$	51.00 m $\Omega$ $\angle 12.36^\circ$
Total impedance of the inductor coil in the <i>loaded</i> sensor	$Z_I = Z_{I,0} + \Delta Z_I$	11 515 m $\Omega$ $\angle 89.66^\circ$
Characteristic impedance of the oscillatory circuit of the <i>loaded</i> sensor	$\rho = \text{Im } Z_I$	11 514 m $\Omega$
Estimate for quality factor of the <i>loaded</i> sensor	$Q = \rho / \text{Re } Z_I$	170
Resonant resistance of the sensor parallel oscillatory circuit when the sensor is <i>loaded</i>	$R_{in} = Q \rho$	1.61 k $\Omega$
Parallel equivalent of the resonant burden resistance of the sensor oscillatory circuit when the sensor is <i>loaded</i>	$R_{brd\text{ prl}}$	2.66 k $\Omega$

\* If not marked otherwise, the values are results of model calculations.

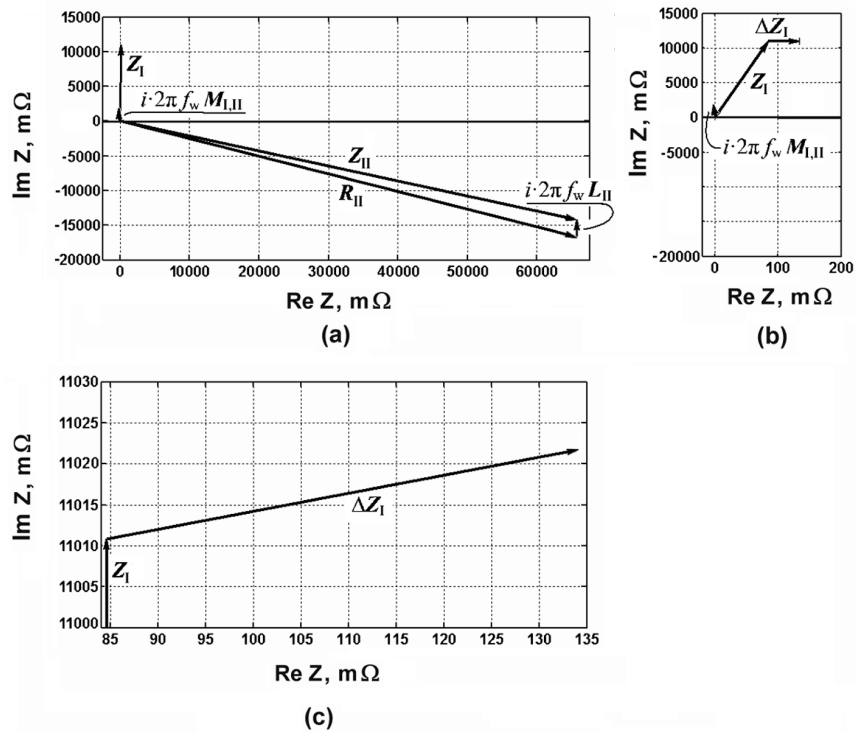


**Fig. 6.** Series of phasor diagrams, with increasing magnification, of impedance quantities related to the genesis of the FouCG signal. The basic set-up of the model: (a) – characteristics of the secondary circuit, the scales of real and imaginary axes are equal; (b) – region of the  $\Delta Z_1$ , the real axis is zoomed; (c) – the same, the real axis is zoomed more. Only Figs 6a and 6c represent true phasors angles.

In Fig. 6, the phasor diagram of impedance quantities, related to the genesis of the FouCG signal, is presented. Figure 6a presents the characteristics of the secondary circuit. A peculiarity of the inductor, loaded by an object, composed of biological tissues, can be noticed. As the impedance, associated with the complex inductance  $L_{II^\circ}$  of the secondary circuit, is small and close to the pure inductive one, the secondary circuit impedance  $Z_{II}$  is mainly determined by the burden impedance  $R_{II^\circ}$ . Due to the presence of the imaginary component in the burden impedance  $R_{II^\circ}$ , the modulus of the secondary circuit impedance  $Z_{II}$  is even a bit less than the modulus of  $R_{II}$  (Fig. 6a).

In Fig. 6b, the real axis is zoomed and the reflected impedance  $\Delta Z_1$  becomes visible.

#### 4.2. Comparative calculation of the model with FEM

To achieve data for the verification of the model, the FEM calculation of its most important characteristics was carried out using the COMSOL Multiphysics software package (AC/DC module, axial symmetry 2D space and quasi-static-magnetic calculation mode with azimuthal induction currents). The geometry of

the model was exactly the same as in the main model, except for an additional domain of air around the components. Presence of axial symmetry allowed the use of 2D simulation mode instead of the 3D mode and that enabled us to calculate certain regions with a very high element density. The total number of elements was around 419 000. The highest element density was required on the edges of the inductor coil with an extremely shallow skin depth. Copper was used for the coil as a material with  $60 \times 10^6$  S/m electric conductivity. This, along with the high frequency of 7.686 MHz, produced the skin depth of  $23.4 \mu\text{m}$ . The triangular finite element mesh was created with variable mesh density (Fig. 7) and the elements in the edges of the current carrying coil wire were defined with a precision of  $1 \mu\text{m}$  (at least 20 times smaller than the skin depth). The element size decreased to  $0.1 \mu\text{m}$  in the corners of the current wire.

The material properties in COMSOL Multiphysics were calculated from the complex impedivity values that were used in the main numerical model. The actual values are given in Table 4.

The dielectric permittivity of metals is known to be of a high negative value, but in this simulation it does not play any role, because the conductivity is high enough to mask any dielectric properties. The value for relative permittivity of copper wire is chosen 1 for convenience without any ill effects.

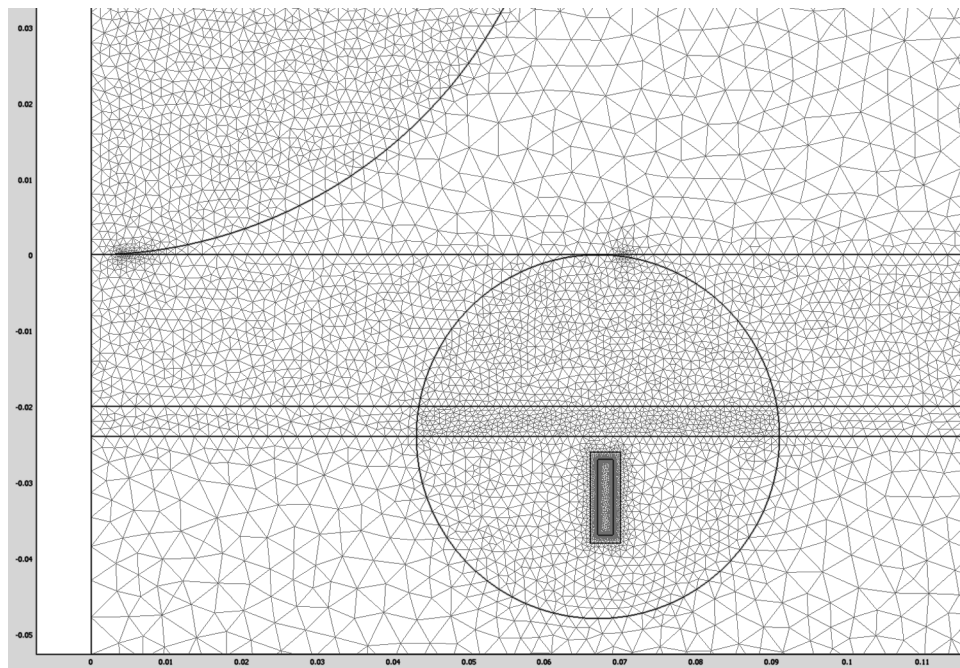


**Fig. 7.** Visualization of the triangular mesh of the FEM model, merely parts of the main components are shown. Symmetry axis is on the left side, directed upwards from the 0-position of the horizontal scale. There is an additional circle surrounding the coil cross-section, for meshing control purposes only.

**Table 4.** Electric properties of the materials used in the COMSOL Multiphysics calculation

Material/tissue domain	Conductivity	Relative dielectric permittivity
Heart	0.7222 S/m	386.18
Lung	0.3034 S/m	186.74
Chest wall	0.3009 S/m	173.11
Copper wire	60 MS/m	1

The simulation gave following results for the coil impedance and the reflected impedance:

impedance of the unloaded inductor coil –  $Z_{1,0} = 12.679079 \Omega \angle 89.92^\circ$ ,  
 impedance of the inductor coil loaded by the disk model of thorax –  
 $Z_1 = 12.689975 \Omega \angle 89.69^\circ$ ,  
 the reflected impedance –  $\Delta Z_1 = Z_1 - Z_{1,0} = 51.463 \text{ m}\Omega \angle 12.03^\circ$ .

The inductor coil impedance value in the unloaded sensor,  $Z_{1,0}$ , from FEM calculation slightly differs from the result of the main model calculation (Table 3)  $Z_{1,0} = 11.504 \text{ m}\Omega \angle 89.92^\circ$ . The difference is mainly due to the inductive reactance or, consequently, due to the calculation of the inductance of the coil, which overwhelmingly determines the impedance. Still, the results of both calculations agree sufficiently well. The value of the reflected impedance from Multiphysics' results is in good agreement with the result of the main model calculation  $\Delta Z_1 = 51.00 \text{ m}\Omega \angle 12.36^\circ$ .

Thus, we can conclude that the values of the reflected impedance, calculated for the same model using two methods, agree well.

## 5. ANALYSIS

### 5.1. General features

The static impedivities, assigned to the three thoracic tissues in the model (Table 2), have phase angles in a rather narrow sector, from  $-8^\circ$  to  $-15^\circ$ . The consequence is that Fig. 6 is roughly true for all the set-ups of the model, except for the pure active impedivity case. Of all the quantities, which became complex due to the biotissues involved (i.e.  $R_{II}$ ,  $L_{II}$  and  $M_{I,II}$ ), the  $R_{II}$  is the most deviated ( $\cong -15^\circ$ ) from a real number. The deviations of the inductances,  $L_{II}$  and  $M_{I,II}$ , are much smaller, i.e., they are not far from conventional inductances. Thus the reactive component of the impedivity of biotissues mainly influences the “complex resistive” properties of the object, inductances are mostly determined by geometry. This result is consistent with what could be expected. Through  $R_{II}$ , also  $Z_{II}$  gets main part of its deviation from an active resistance (Fig. 6).

### 5.2. Comparison with actual measurements

The results of calculation can be compared with experimental data. The reflected impedance  $\Delta Z_1$  can be watched through the reactions of the sensor output to attaching the sensor to the human body.

Appropriate data [9] have been obtained in experiments with the example sensor incorporated in the sample Foucault cardiograph [3]. In the experiments, calibration of the device was effected using parallel resistive loading. For the calibration, precise resistors were connected in parallel with the unloaded sensor coil and corresponding reactions in the Foucault cardiograph output were obtained. After this, the sensor was attached to 4 normal volunteer male subjects and a collection of reactions was recorded.

Putting the results of the calibration and the data from human volunteers into the same diagram (Fig. 8) enabled us to get estimates of the parallel equivalent resistance.

The result of this experiment was that the parallel resistive equivalent of the human body had values in the range from 1.3 to 2.3 kΩ for the persons studied.

In our model calculations we have found that the reflected impedance  $\Delta Z_1$  in the primary circuit has a small imaginary inductive part and much greater real (series resistive) part. Due to the self-oscillatory construction of the example Foucault cardiograph, the parallel oscillatory circuit, comprising the sensor, works permanently at resonance conditions. The inductive component of  $\Delta Z_1$  forces the oscillation frequency of the loaded sensor,  $f_w$ , to fall below the resonance frequency of the unloaded sensor. The resistive component affects the quality factor of the sensor. Knowing the quality factor of both the unloaded sensor ( $Q_0 = 644$ ) and the loaded sensor ( $Q = 170$ , Table 3), we can calculate the parallel equivalent burden resistance in the primary oscillatory circuit of the sensor:

$$R_{\text{brd prl}} = \frac{1}{\frac{1}{Q} - \frac{1}{Q_0}}. \quad (11)$$

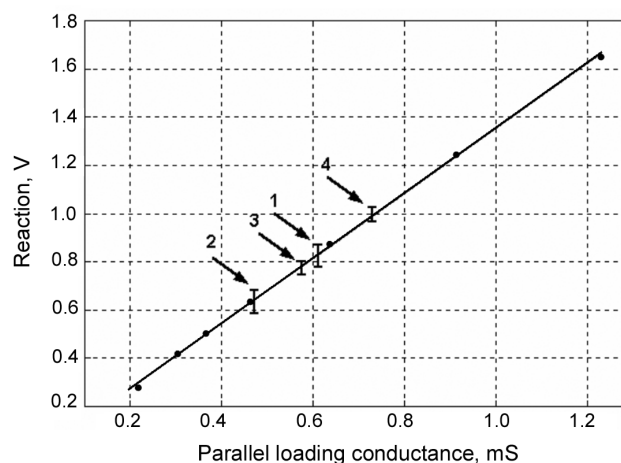


**Fig. 8.** Estimation of the parallel equivalent resistance for humans. Dots – the data of calibration of the Foucault cardiograph; the numbered arrows point at the data of volunteers studied.

This is actually just a model estimate of the equivalent parallel resistance for the human body. A calculation, using Eq. (11), produces  $R_{\text{brd prl}} = 2.66 \text{ k}\Omega$ . This result is sufficiently consistent with the experimental findings.

### 5.3. Study of poorly known thoracic wall impedivity

In Figs 9 and 10, results of the variation of the thoracic front wall impedivity in the model can be seen. Evidently, the effect of this variation appears mostly in the phase of the secondary circuit impedance  $Z_{\text{II}}$  and, consequently, in the phase of the primary circuit reflected impedance  $\Delta Z_1$ . Even the model with fully active impedivities gives the moduli of both impedances in the same value ranges.

Although the modulus of the thoracic wall impedivity had been varied from the basic value  $3.23 \text{ }\Omega\cdot\text{m} \angle -13.8^\circ$  up to the muscular impedivity  $1.63 \text{ }\Omega\cdot\text{m} \angle -8.4^\circ$ , the corresponding variations of  $Z_{\text{II}}$  and  $\Delta Z_1$  were more limited:  $Z_{\text{II}}$  changed from  $67.26 \text{ }\Omega \angle -12.2^\circ$  to  $66.52 \text{ }\Omega \angle -10.7^\circ$ , and  $\Delta Z_1$  changed from  $50.57 \text{ m}\Omega \angle 12.4^\circ$  to  $52.12 \text{ }\Omega \angle 10.8^\circ$ .

Thus, the reasonable variation of the thoracic wall impedivity can neither change the properties of the model qualitatively nor even influence the numerical values significantly. The most noticeable of its influences is the influence on the phases of  $Z_{\text{II}}$  and  $\Delta Z_1$ , which shall be taken as the indicator of uncertainty of those phase values due to modelling.

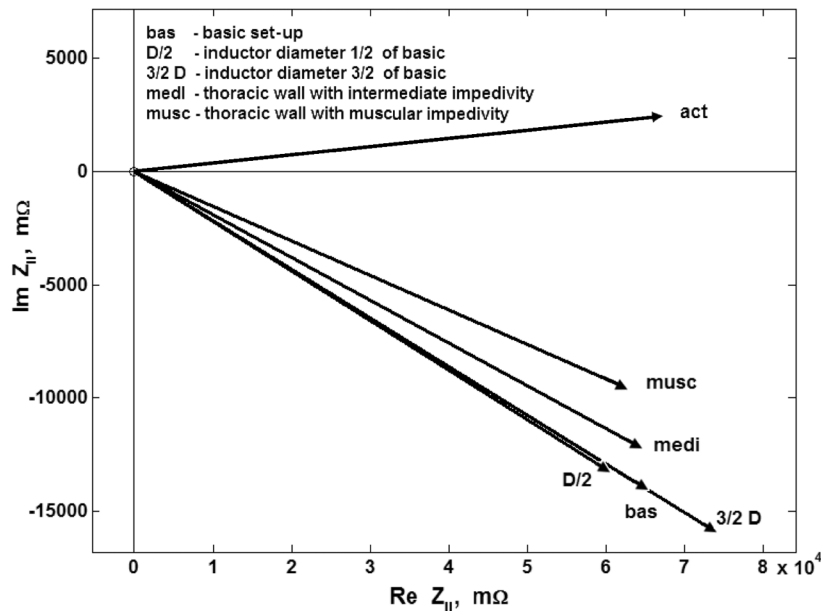


Fig. 9. Phasor diagram of the secondary circuit impedances  $Z_{\text{II}}$  for the studied set-ups of the model.

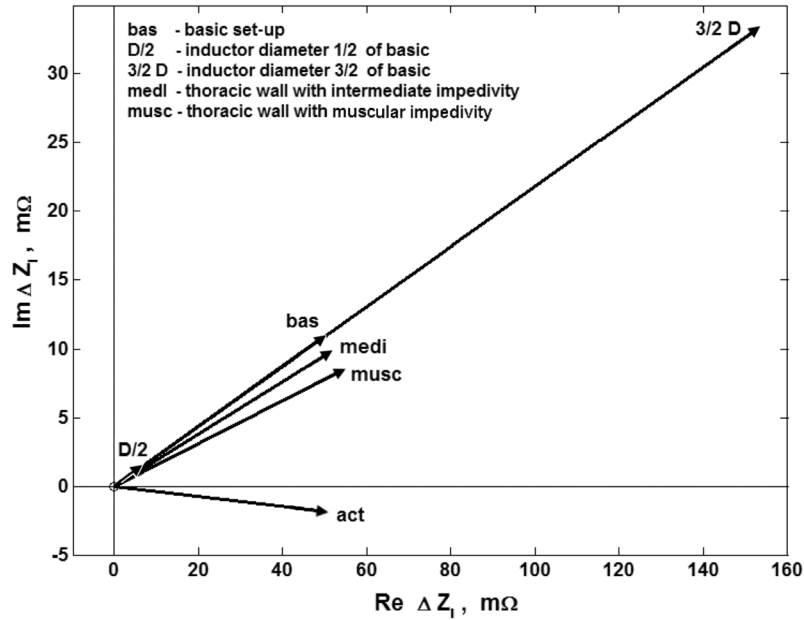


Fig. 10. Phasor diagram of the reflected impedances  $\Delta Z_I$  for the studied set-ups of the model.

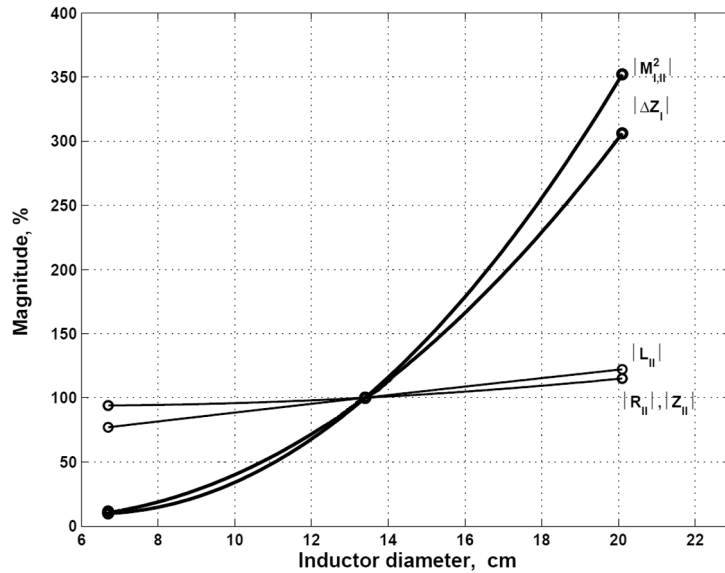
#### 5.4. Influence of the inductor diameter on its efficiency

Figure 10 demonstrates the strong effect of variation of the inductor diameter upon the reflected impedance  $\Delta Z_I$  (see the cases D/2 and 3/2 D).

As a result of model calculations, we can state that by the variation of the inductor diameter, the factors  $M_{I,II}$ ,  $R_{II}$ ,  $L_{II}$ , which act in forming of the reflected impedance  $\Delta Z_I$  (recall Eq. (10)), almost retain their phase angle values. For the inductances,  $M_{I,II}$  and  $L_{II}$ , those angles are rather small (about  $0.1^\circ$  for  $M_{I,II}$ , and from  $0.5^\circ$  to  $0.3^\circ$  for  $L_{II}$ , both positive and decreasing with the increase of the inductor diameter). As is natural, the secondary circuit „burden impedance“  $R_{II}$  shows greater deviation from its prototype – the burden resistance – exhibiting a stable phase angle of  $-14^\circ$ .

Thus the changing of these factors due to the variation of the diameter of the inductor can be described by presenting their moduli, as has been done in Fig. 11. All the quantities there have been normalized to 100% for the basic value of the diameter.

As  $Z_{II}$  consists mostly of  $R_{II}$ , the relative variations of  $R_{II}$  and  $Z_{II}$  are very close to each other. Since  $M_{I,II}^2$  and  $Z_{II}$  are divided in Eq. (10), the relative variation of the reflected impedance  $\Delta Z_I$  is given by the difference of their relative variations. The factor of these two, which varies most, is  $M_{I,II}^2$ , which grows monotonically with the growth in diameter of the inductor, in the present case approximately as a quadratic function. This well-known feature is the reason why similar growth of  $|\Delta Z_I|$  can be seen in Fig. 11. Meanwhile, the growth of  $R_{II}$  as *antagonist* slightly decreases the growth of  $|\Delta Z_I|$ .



**Fig. 11.** Percentage changing of the moduli of the reflected impedance  $\Delta Z_I$  and its factors when the diameter of the inductor is varied. Circles indicate the values obtained in model calculations, the curves being quadratic interpolations.

Increase of the reflected impedance leads to consequent increase of its variation in the process of heart volume pulsation. Thus to increase the magnitude of the signal and also the signal-to-noise ratio, it would be instrumental to use inductors with larger diameters. Unfortunately, this is limited by the less comfortable use of the sensor.

## 6. DISCUSSION

The developed axisymmetric model can serve as an instrument for studying general problems of FouCG origination and measurement. The geometrical and electromagnetic simplicity of the present model ensures that the most important features of FouCG can be studied in the simple, uncombined, state. Due to such radical simplifications, the model does not enable detailed simulation. The latter shall be the area of FEM-based modelling.

In comparison with possible FEM realizations (one of which, based on the COMSOL Multiphysics software, was used in the present study) our semi-analytical realization of the model has following advantages.

It enables the description of modelled situation in terminology used for lumped systems, thus unifying the description of the measurement object and the electronic circuits used to measure it; the theory and the properties of the elements, used in the building of this lumped model, are familiar to engineers.



The connections between the lumped characteristics of the secondary and primary circuits characteristics ( $R_{II}$ ,  $L_{II}$ ,  $M_{I,II}$ ,  $\Delta Z_I$ ) of the system have been found analytically, thus in calculations the integrations of distributed fields are replaced with summations over secondary circuit elementary coils. For instance, to find  $\Delta Z_I$  with the FEM method, the  $Z_I$  values for the unloaded and loaded inductor are integrated and then subtracted (two large but close numbers); using our approach it can be directly calculated without subtraction. Our realization runs in a general-purpose computing medium (the MATLAB base module).

There is an important question, which often arises by modelling the inductive measurement systems – at which stage in the calculations the iteration of the magnetic field can be stopped. Generally, there shall be an iterative calculation process to take into account that the induced eddy currents themselves produce a contribution into the magnetic field, which induces them. In the case of a biological object, the impedivities of the tissues are fairly high in comparison with metals, which enables a small number of iterations.

In the present approach we calculate the electromagnetic interactions using conventional and well-tested approximation formulae for inductances and mutual inductances, which do not require iterating. The stage of calculation, in which iterating is necessary, is the calculation of the distribution of eddy currents induced by the common magnetic field of the inductor and the elementary coils in the object. This distribution determines the weights  $K_i$  for the calculation of resistances, inductances and mutual inductances. We have succeeded with no iterations, counting only once the magnetic field, generated by the inductor coil. This is justified both by the arrangement of the Foucault cardiograph – the inductor is fed by a constant current generator – as well as by the fact that the inductive reactances of the elementary coils are small – less than 0.05% of the corresponding capacitive reactances, the latter being determined by the material of the coils. As we saw above, the final result of model calculation of  $\Delta Z_I$  agrees with the result of calculation using the FEM method and also with the experimental result.

Another finding (which was expected) is connected with the necessity of using complex-numerical values for the impedivities of the tissues. The presence of the inductances and mutual inductances necessarily leads to using complex-numerical calculation in the model, still the tissues could be characterized by real-numerical (active) impedivities. This leads to results having moduli close to the corresponding ones when the model calculations are done with complex-valued impedivities. The phase angles of the results are different in this case, but if the phases are not needed (e.g., if calculations are done for a system with the amplitude detection of the carrier frequency signal), then active description of tissue impedivities is sufficient.

It must be noted that skin effect in the inductor coil strongly affects the calculation through its influence on the resistance of the inductor. It should be carefully taken into account.

All the calculations of the model, described above, are done for the working frequency  $f_w = 7.686$  MHz. As the output of the sensor is proportional to  $f_w^2$  (recall Eq. (10)), it shall be rather hard to get a signal of a satisfactory magnitude at working frequencies, which are much lower. Alternatively, raising the working frequency can significantly change the situation – the contribution of the eddy currents in the total magnetic field of the system grows and several simplifications become invalid.

## 7. CONCLUSIONS

The presented investigation has led to the following conclusions about the single-coil FouCG sensor, working at a frequency in the vicinity of 10 MHz.

1. The Foucault cardiographic sensor, based on a circular inductor, converts the impedance variations in the object attached to it into corresponding simultaneous variations of the reflected impedance  $\Delta Z_I$  in the inductor circuit. This can be considered as the output of this sensor.
2. In a Foucault cardiograph, based on this sensor, it is reasonable to track the modulus of the time variation of the impedance of the inductor coil, as it contains the reflected impedance  $\Delta Z_I$ . It can be done simply using amplitude detection of the voltage oscillations on the inductor fed by a constant current source. Tracking of the real part of the reflected impedance would also be efficient, but not the tracking of the imaginary part.
3. At the calculations of the present model of the sensor-and-body system, which describes the electromagnetic induction effects in terms of self- and mutual inductances, it is reasonable to ignore the self-inductances of the elementary coils at the current distribution calculation. This leads to the omission of the iterative process in the calculation of the inductances.
4. As the main mechanisms of the origination of the Foucault cardiograms, the following two are to be considered. The first is the modulation of the reflected impedance  $\Delta Z_I$  by changing the burden impedance  $R_{II}$  of the body; the second is similar modulation, obtained by changing the mutual impedance  $M_{I,II}$  between the body and the inductor. The mechanisms act as antagonists relatively to one another.
5. If the phase angle of the resulting reflected impedance phasor  $\Delta Z_I$  is not of interest, then even simulation with pure resistive substitutes of the tissue impedivities gives a satisfactory result.

## REFERENCES

1. Tarjan, P. P. and McFee, R. Electrodeless measurements of the effective resistivity of the human torso and head by magnetic induction. *IEEE Trans. Biomed. Eng.*, 1968, **15**, 266–278.
2. Humal, L.-H. and Vedru, J. Physiological measurement based on Foucault principle: set-up of the problem. *Med. Biol. Eng. Comput.*, 1996, **34**, Suppl. 1, Part 2, 183–184.

3. Trolla, J. and Humal, L.-H. Design of a Foucault cardiograph. In *Proc. International Conference on Biomedical Engineering*. Kaunas, Lithuania, 1998. Kaunas, Technologija, 1998, 45–51.
4. Vedru, J. and Gordon, R. Model of an inductive sensor of cardiac activity attached to patient. *J. Phys., Conf. Ser.*, 2010, **224**(1), 012010.
5. Kalantarov, P. L. and Zeitlin, L. A. *Calculation of Inductances: A Handbook*. Energoatomizdat, Leningrad, 1986 (in Russian).
6. Vedru, J. Foucault principle based inductive measurement of bioimpedance variation. In *Proc. XII ICEBI and VEIT*. Gdansk, Poland, 2004, 305–308.
7. Nilsson, J. W. and Riedel, S. A. *Electric Circuits*. Pearson, Prentice Hall, Upper Saddle River, NJ, 2008, 362–363.
8. Gabriel, S., Lau, R. W. and Gabriel, C. The dielectric properties of biological tissues, II. Measurements in the frequency range 10 Hz to 20 GHz. *Phys. Med. Biol.*, 1996, **41**, 2251–2269.
9. Trolla, J. *Building and Study of a Sample Foucault Cardiograph*. MSc Thesis, University of Tartu, 2000.

## **Foucault' kardiogrammi induktiivse sensori modelleerimine**

Jüri Vedru, Rauno Gordon, Leo Henn Humal ja Jaanus Trolla

Foucault' kardiograafia (FouKG) on objekti elektrilise impedantsi muutumise registreerimisel põhinev meetod südame mehaanilise tegevuse jälgimiseks. Meetodi omapäraks on pööris- ehk Foucault' voolude kasutamine sondeeriva voolu rollis. Meetodi arendamine vajab matemaatilist mudelit, mille abil oleks võimalik uurida meetodi kõige põhilisemaid omadusi.

Töös on välja arendatud elektriahelate teoorial põhinev induktiivse sensori arvutimudel FouKG tööolukorras, mil ta on rakendatud inimesele. Inimese keha on modelleeritud sensoripooliga samateljelise pöördsilindrina, milles eristatakse südame, kopsu ja rindkere esiseina piirkondi ning vastavaid kudesid. Bioloogilisele objektile iseloomulikult on kudede elektrilistel eriimpedantsidel kompleksarvulised väärtused. Silindriline sümmeetria võimaldab inimkeha mudelit kirjeldada tihedalt pakitud koaksiaalsete induktiivselt sidestatud rõngaspoolide süsteemina. Viimasele leitakse inimesel läbi viidava mõõtmise tingimustele vastav lihtne ekvivalent ja hinnatakse mõnede süsteemi omaduste mõju FouKG-signaali tekkele.

Mudelil saadud arvtulemusi on võrreldud inimestel mõõdetutega ja sama süsteemi jaoks lõplike elementide meetodil arvatud näitajatega. Mõlemas võrdluses ilmutab mudel võrdlusandmetega head kooskõla.